Spectrochimica Acta Part B 63 (2008) 1274–1282

Contents lists available at ScienceDirect

Spectrochimica Acta Part B

journal homepage: www.elsevier.com/locate/sab

Monte Carlo analysis of the electron thermalization process in the afterglow of a microsecond dc pulsed glow discharge

A. Martín [a], N. Bordel [a], R. Pereiro [b], A. Bogaerts [c,*]

[a] Department of Physics, University of Oviedo, 33007 Oviedo, Spain
[b] Department of Physical and Analytical Chemistry, Faculty of Chemistry, University of Oviedo, 33006 Oviedo, Spain
[c] Department of Chemistry, University of Antwerp, Universiteitsplein 1, B-2610 Wilrijk-Antwerp, Belgium

ARTICLE INFO

Article history:
Received 3 July 2008
Accepted 16 September 2008
Available online 4 October 2008

Keywords:
Pulsed glow discharge
Monte Carlo
Modeling
Electron thermalization

ABSTRACT

A Monte Carlo model is utilized for studying the behavior of electrons in the afterglow of an analytical microsecond dc pulsed glow discharge. This model uses several quantities as input data, such as electric field and potential, ion flux at the cathode, the fast argon ion and atom impact ionization rates, slow electron density, the electrical characterization of the pulse (voltage and current profiles) and temperature profile. These quantities were obtained by earlier Monte Carlo – fluid calculations for a pulsed discharge. Our goal is to study the behavior of the so-called Monte Carlo electrons (i.e., those electrons created at the cathode or by ionization collisions in the plasma which are followed by using the Monte Carlo model) from their origin to the moment when they are absorbed at the cell walls or when they have lost their energy by collisions (being transferred to the group of slow electrons) in the afterglow of the pulsed discharge. The thermalization of the electrons is a phenomenon where the electron-electron Coulomb collisions acquire a special importance. Indeed, in the afterglow the cross sections of the other electron reactions taken into account in the model are very low, because of the very low electron energy. We study the electron energy distributions at several times during and after the pulse and at several positions in the plasma cell, focusing on the thermalization and on the behavior of the electrons in the afterglow. Also, the time evolution of the rates of the various collision processes, the average electron energy, the densities of Monte Carlo and slow electrons and the ionization degree are investigated.

1. Introduction

Pulsed glow discharges (PGDs) have been found more advantageous than non-pulsed glow discharges for many analytical applications. In fact, PGDs can be used as analytical spectrochemical sources for mass spectrometry [1,2], optical emission spectrometry [3,4], atomic absorption and fluorescence spectrometry [5,6]. The most important characteristics of pulsed discharges are a higher peak power during the pulse compared with the continuous mode due to a high instantaneous current, which implies comparatively higher analyte signals, for the same average power, than those observed using conventional direct current (dc) discharges [7,8], whilst the background noise can be reduced [4]. If a time-gated detection system is employed, (e.g. a time-of-flight mass analyzer), the pulsed discharge ions coming from the sample can be discriminated from the ions coming from the discharge gas or the carrier gas [9]. In this way, difficult isobaric interferences, as ^{40}Ar and ^{40}Ca [10] could be avoided. The reason is related to the different times at which these two types of charged species are created in the pulsed discharge. This opens the possibility of "filtering" undesirable ions by using a suitable selection of the pulse parameters (width and frequency) and the detection delay time in the mass analyzer [11].

PGDs can be powered in a wide range of pulse widths and frequencies. However, the frequency is usually lower than 1 kHz (normally between 200–600 Hz) for analytical applications. PGDs can be split into two groups according to the pulse width: millisecond pulsed glow discharges, characterized by duty cycles about 25% (i.e., the ratio of pulse duration versus total pulse on and off time, expressed as a percentage) and microsecond pulsed glow discharges with duty cycles about 5%. Those two kinds of pulsed discharges offer different analytical features: the microsecond pulsed regime can provide higher analyte signals and is ideal for material analysis; on the other hand, due to the different temporal characteristics in the glow discharge plasma, the millisecond regime enables atomic, molecular or structural information, (i.e. speciation analysis capability) in a better way than the microsecond pulsed discharge does [12,13].

Another interesting property of PGDs is related to the low average sputtering rate [7] (as the average power integrated over a period is very low) and the negligible heating effect on the cathode. These facts are most advantageous in the field of thin films analysis [14–16]. PGDs have been produced by using hollow cathode and Grimm lamps, which have been coupled to optical emission and mass spectrometry.

Finally, high-voltage PGDs (tens of kV) have proved to be a potentially effective surface treatment technique, which can be placed

* Corresponding author. Tel.: +32 3 820 2377.
E-mail address: annemie.bogaerts@ua.ac.be (A. Bogaerts).

0584-8547/$ – see front matter © 2008 Elsevier B.V. All rights reserved.
doi:10.1016/j.sab.2008.09.012

between the low voltage (~1 kV) and high pressure conditions used in conventional plasma nitriding and the high-voltage (up to 100 kV) and low pressure conditions utilized in plasma immersion ion implantation (PIII) [17].

PGDs offer a different behaviour than seen for steady state GDs, in terms of the temporal response (during and after the pulse) assigned to PGDs. It is known that the intensities of optical emission lines show a peak in the afterglow (i.e., when the voltage is switched off) [18,19]. In the literature, this is attributed to electron-ion recombination and consequently to the existence of a large number of highly excited as well as metastable argon states. Furthermore, the increase of the metastable argon density in the afterglow enhances Penning ionization (responsible for most of the ionization of the sputtered atoms) [20]. However this explanation has not been quantitatively confirmed yet by numerical models, since electron and argon ion densities and the recombination rate coefficients appear to be too low to account for this process. Nevertheless, from a recent work by Bogaerts [21], it is predicted that dissociative recombination between Ar_2^+ ions and electrons might be responsible for this after-peak formation.

As voltage termination results in electron thermalization and plasma recombination, we focus here on how this electron thermalization is accomplished in the afterglow, studying mainly the electron energy distributions as a function of time (during the pulse and in the afterglow). For this reason, the proposed Monte Carlo (MC) model must include a realistic electron–electron (e–e) collisions treatment, because of the importance of this process and its contribution to the electron energy in the afterglow.

2. Description of the model

The electron MC model utilized in this work is based on a hybrid MC — fluid modeling network described previously and developed for PGDs [22–24]. The following results obtained with the hybrid model, are used as input in the simulation: electric field and potential distribution, the ionization rates due to fast Ar^+ ions and fast Ar atoms, slow electron densities, and the flux of ions at the cathode.

In our MC model we include the following reactions [25–28]: excitation and ionization of argon atoms, elastic collisions with argon atoms and (e–e) collisions. Fig. 1 illustrates the cross sections of these processes as a function of the energy. Besides these reactions, we also consider dissociative recombination and collisional-radiative recombination because these processes are important in the afterglow [24]. The rate coefficients k_{dr} and k_{crr} respectively for both recombination mechanisms as a function of the electron temperature, T_e, are:

i. Dissociative recombination [29,30]: $Ar_2^+ + e^- \rightarrow Ar^* + Ar$

$$k_{dr} = 9\cdot10^{-7}\left(\frac{T_e}{300}\right)^{-0.61}\left[cm^3s^{-1}\right]$$

The cross section, σ, assigned to this recombination is calculated as follows:

$$\sigma\cdot n = \frac{k_{dr}}{v_{th}}\cdot N_{Ar_2^+}\left(N_{Ar_2^+}\simeq N_{e^-}\cdot 1/3\right)$$

ii. Collisional-radiative recombination [31]: $e^- + Ar^+ + e^- \rightarrow Ar^* + e^-$

$$k_{crr} = 10^{-19}\left(\frac{T_e}{300}\right)^{-9/2}\left[cm^6s^{-1}\right]$$

The cross section derived from this kind of recombination is calculated as:

$$\sigma\cdot n = \frac{k_{crr}}{v_{th}}\cdot N_{Ar^+}\cdot N_{e^-}\left(N_{Ar^+}\simeq N_{e^-}\cdot 2/3\right)$$

In both recombination processes, T_e is given in (K), v_{th} is the thermal velocity and N_{Ar+}, $N_{Ar_2^+}$ and N_{e^-} are the Ar^+, Ar_2^+ and MC electron densities in cm^{-3}. The densities of the two argon ions (Ar_2^+ and Ar^+) are estimated from the electron, Ar^+ and Ar_2^+ densities calculated by Bogaerts [21]. Here, recombination has been expressed as the product of $\sigma\cdot n$ (where n represents the density of the target particles in this notation) in order to keep a parallelism with $\sigma\cdot n$ for the collisions with Ar atoms and (e–e) collisions.

Including (e–e) collisions in numerical models is more complicated than the other processes studied here, due to the nonlinear character of the interactions: i.e., it is a long-range interaction and the cross section is dependent on the relative velocity between the two colliding electrons. Fortunately, studies based on MC simulations where the (e–e) collisions are investigated [32–34], can be found in the literature. We selected the method described by Alkaa et al [35,36] where the (e–e) collisions are treated in the MC model as collisions of electrons with heavy particles (atoms and molecules), with electrons colliding with an energy-resolved electron fluid in the same way as they collide with the neutral fluid.

The (e–e) collision technique implemented in our approach can be summarized in the following way: to calculate the binary interaction between two identical particles it is necessary to know the velocity of the electrons before the collision. Such velocities are directly calculated in the MC algorithm. The classical Coulomb angular differential cross section is replaced by the momentum transfer cross section because the effect of (e–e) collisions is less important as the scattering angle is near zero. The momentum transfer cross section σ_{mee} is defined as [37]:

$$\sigma_{mee}(v_r) = 2\pi b_0^2 \ln\frac{2}{1-\cos\chi_{min}} \quad (1)$$

where b_0 is the impact parameter and χ_{min} is the minimum scattering angle [35]:

$$b_0 = \frac{e^2}{4\pi\varepsilon_0\mu v_r^2} \quad (2)$$

$$\cos\chi_{min} = \frac{\lambda_D^2 - b_0^2}{\lambda_D^2 + b_0^2} \quad (3)$$

λ_D is the Debye length, μ is the reduced electron mass ($m_e/2$) and v_r is the relative velocity between the two colliding electrons

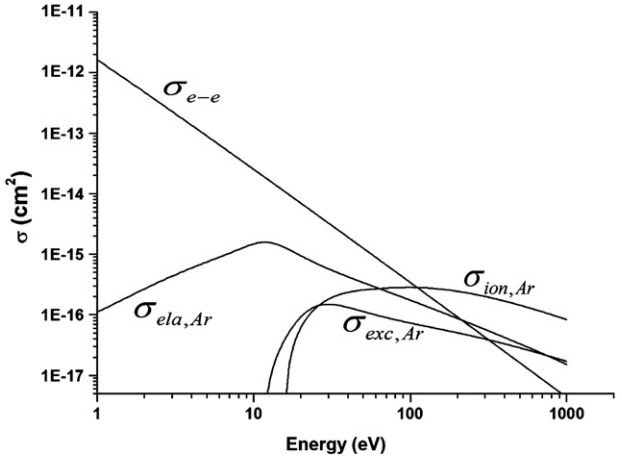

Fig. 1. Cross sections of the electron collision processes incorporated in the model, as a function of the electron energy.

(defined by test electron and target electron), calculated in the following way. The components of the velocity as well as the energy of the test electron *before* the collision at a time t_c (i.e., $v_x^b(t_c)$, $v_y^b(t_c)$, $v_z^b(t_c)$, $E^b(t_c)$) are explicitly determined in the MC code. On the other hand, the velocity components and the energy of the target electron (Eq. (4)) at the same time t_c (i.e., $v_{xt}(t_c)$, $v_{yt}(t_c)$, $v_{zt}(t_c)$, $E_t(t_c)$) are calculated by using three pseudo-random numbers (RN1, RN2, RN3), and based on the energy and angular distribution function ($f(t_c, z(t_c), r(t_c), E)$ and $f(t_c, z(t_c), r(t_c), E, \theta)$) of all electrons previously followed at each time-step during the simulation.

$$\begin{aligned} v_{xt}(t_c) &= v_t \sin\theta_t \cos\varphi_t \\ v_{yt}(t_c) &= v_t \sin\theta_t \sin\varphi_t \\ v_{zt}(t_c) &= v_t \cos\theta_t \\ v_t &= \sqrt{\frac{2E_t}{m_e}} \end{aligned} \tag{4}$$

The energy E_t of an hypothetical target electron is calculated based on the distribution function $f(t_c, z(t_c), r(t_c), E)$ and by defining a pseudo-random number RN1:

$$\mathrm{RN1} = \frac{\int_0^{E_t} f(t_c, z(t_c), r(t_c), E)dE}{\int_0^{E_{max}} f(t_c, z(t_c), r(t_c), E)dE} \tag{5}$$

Afterwards, the polar angle θ_t of the same target electron is calculated from the angular distribution function, $f(t_c, z(t_c), r(t_c), E_t, \theta)$, which takes into account the target electron energy, E_t, determined above. A second pseudo-random number is generated and a similar integration is carried out:

$$\mathrm{RN2} = \frac{\int_0^{\theta_t} f(t_c, z(t_c), r(t_c), E_t, \theta)d\theta}{\int_0^{\pi} f(t_c, z(t_c), r(t_c), E_t, \theta)d\theta} \tag{6}$$

If an electron–electron collision occurs, E_t and θ_t are calculated in this way from the energy and angular distribution of the electrons followed at the moment of the collision. The method employed to solve the integrals is the MC acceptance-rejection method [38] with a maximum energy equal to 2000 eV (E_{max}). This method requires a high computational time in order to give a good approximation to the integrations. A value of 95% of accuracy was adopted in the calculation. Both values of E_t and θ_t are used until the end of the time-step or until a new (e–e) collision is produced. The azimuthal angle of the target electron φ_t is easily determined as $\varphi_t = 2\pi\mathrm{RN3}$. Finally, from these operations we can calculate the relative velocity between the test and target electron (Eq. (7)), and therefore the momentum transfer cross-section (Eq. (1)).

$$\begin{aligned} v_{rx} &= v_x^b(t_c) - v_{xt}(t_c) \\ v_{ry} &= v_y^b(t_c) - v_{yt}(t_c) \\ v_{rz} &= v_z^b(t_c) - v_{zt}(t_c) \\ v_r &= \sqrt{v_{rx}^2 + v_{ry}^2 + v_{rz}^2} \end{aligned} \tag{7}$$

The velocity components and the energy of the test electron *after* the (e–e) collision are calculated by:

$$\begin{aligned} v_x^a(t_c) &= 0.5\left(v_x^b(t_c) + v_{xt}(t_c) + v_{r'x}(t_c)\right) \\ v_y^a(t_c) &= 0.5\left(v_y^b(t_c) + v_{yt}(t_c) + v_{r'y}(t_c)\right) \\ v_z^a(t_c) &= 0.5\left(v_z^b(t_c) + v_{zt}(t_c) + v_{r'z}(t_c)\right) \\ E^a(t_c) &= 0.5 \cdot m_e \cdot \left(v_{r'x}^2(t_c) + v_{r'x}^2(t_c) + v_{r'x}^2(t_c)\right) \end{aligned} \tag{8}$$

where $v_{r'x}(t_c)$, $v_{r'y}(t_c)$, $v_{r'z}(t_c)$ are the relative velocities (Eq. (7)) after their transformation from the particle scattering frame of reference to the laboratory frame of reference. These expressions (Eq. (8)) have been previously derived by Alkaa et al. [35,36].

Because the MC method is a technique where statistics are important, it is convenient to ensure a high electron population during the whole simulation. This is specially true after the pulse termination, where the current and voltage are nearly extinguished (resulting in a reduced number of electrons emitted from the cathode) and when the electron thermalization begins to be important. For reducing the computational time, we include two electron weight factors: one is related to the energy of electrons [39] and the other is related to the number of electrons that will be followed at each time. The number of electrons created at the cathode is reduced by a certain factor, in such a way that the initial number of electrons to follow is fixed (of course, this initial number would increase due to ionization in the plasma), and the ratio between the real number of electrons and those followed is updated at each time-step. Several quantities, such as the MC electron densities, ionization, excitation and elastic collision rates are adapted at the end of the time-step by the corresponding factor.

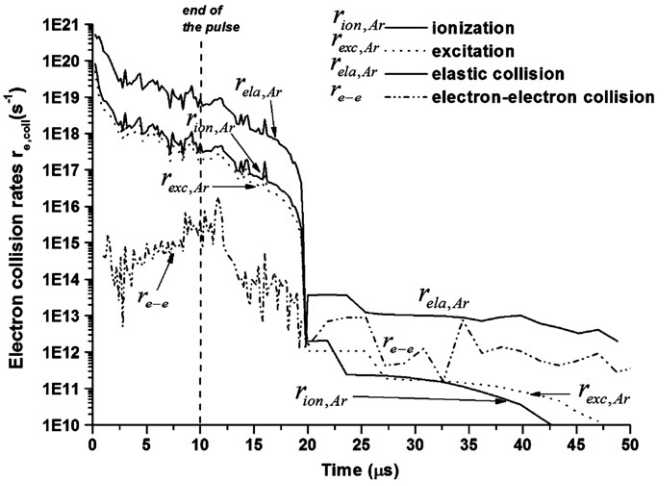

Fig. 3. Calculated collision rates, integrated over the entire discharge region, of the electron collisions, as a function of time during and after the pulse: ionization ($e^- + Ar^0 \rightarrow Ar^+ + 2e^-$), excitation ($e^- + Ar^0 \rightarrow Ar^{0*} + e^-$), elastic collision ($e^- + Ar^0 \rightarrow Ar^0 + e^-$), electron–electron collision ($e^-_{test} + e^-_{target} \rightarrow e^-_{test} + e^-_{target}$). The end of the pulse is indicated by vertical dashed line.

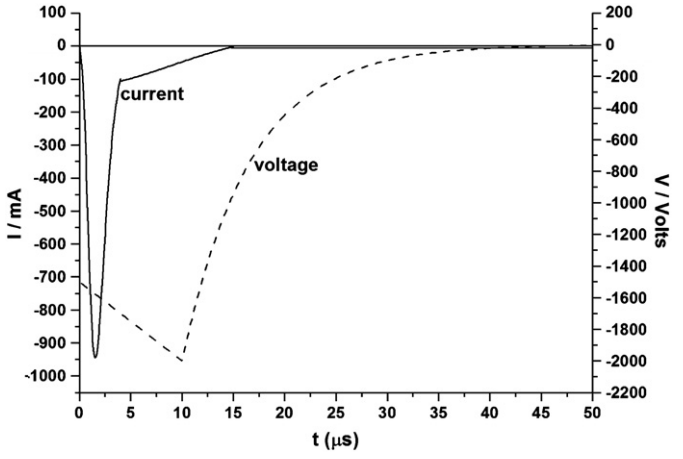

Fig. 2. Current (solid line) and voltage (dashed line) as a function of time during and after the pulse at a gas pressure of 3 Torr.

3. Results and discussion

We assume the same cell geometry and pulse parameters (width, frequency and voltage), as in ref. [22,23]: 10 μs pulse width with a

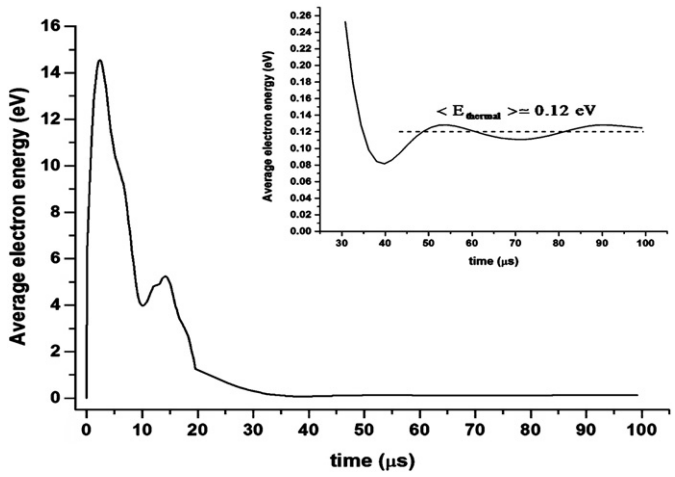

Fig. 4. Average electron energy calculated from all the electrons followed in the plasma cell, taking into account the different weighting factors at different positions in the plasma, according to the statistical weight and the different electron density profile at each point in the cell (grid).

repetition frequency of 200 Hz and applied pulse voltage of −2 kV. The cell geometry is based on the Grimm-type source where it is assumed to be a simple cylinder, with 4 mm diameter and 2.6 cm length. We adopted a gas temperature as a function of time [22,40] and an electrical current profile calculated previously [22]. The pulse electrical characteristics are plotted in Fig. 2.

3.1. Electron thermalization

The electron thermalization takes place when the electrons cannot gain energy anymore from the electric field. The latter is indeed absent in the afterglow (i.e., several microseconds after pulse termination). In Fig. 3 the rates of elastic collisions, ionization and excitation of argon atoms, as well as electron–electron collisions, integrated over the entire discharge, are plotted as a function of time during and after the pulse. Before the pulse termination (i.e., during the first 10 μs), the ionization, excitation and elastic collision rates evolve in the same way: they decrease gradually, although the elastic collision rate is nearly one order of magnitude higher. On the other hand, the (e–e) collision rate slightly increases, and the difference between (e–e) collision and elastic collision rates, which initially is about 6 orders of magnitude, has been reduced at the end of the pulse (at 10 μs) to only 3 orders of magnitude. In the early afterglow (i.e., the next 10 μs after the pulse termination), the ionization, excitation and elastic collision rates continue to decrease, but close to 20 μs they drop abruptly about 4–5 orders of magnitude. The (e–e) collision rate decreases less drastically and at 20 μs the four electron collision rates are practically the same. From this point, the excitation and ionization rates decrease

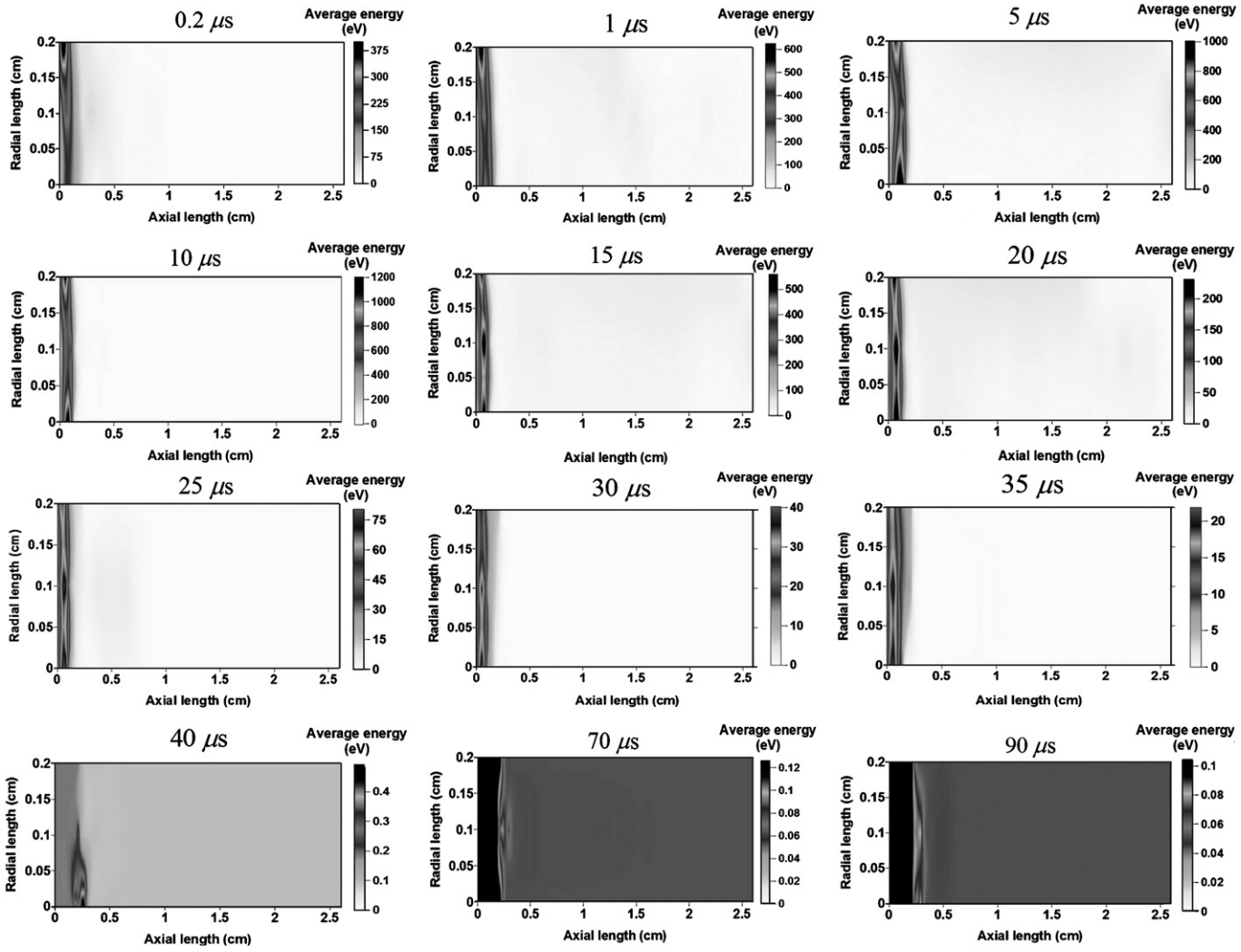

Fig. 5. Spatial distribution of the average electron energy, plotted at different times during and after the pulse.

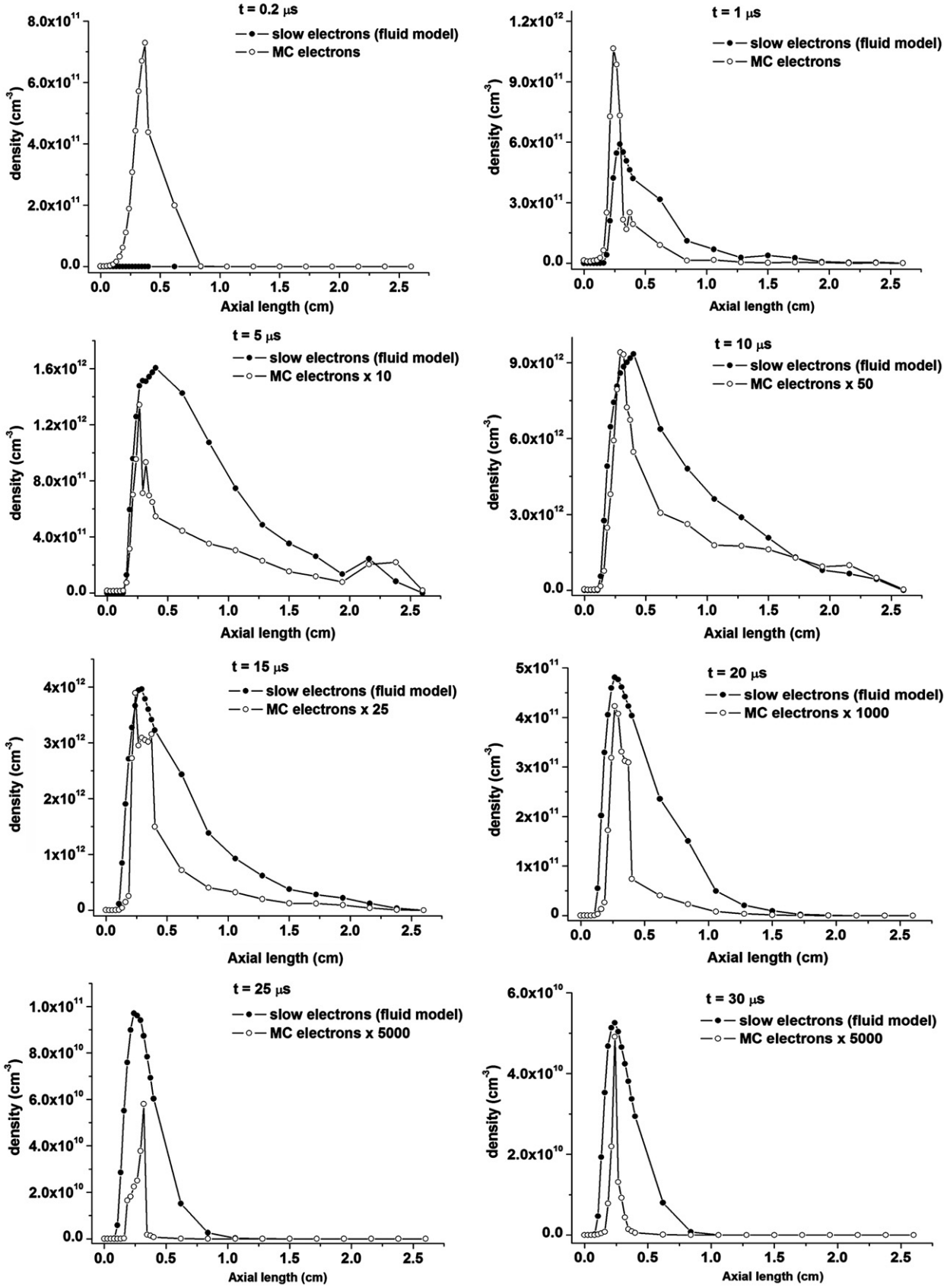

Fig. 6. Slow and MC electron axial density distributions calculated by averaging over all radial positions at different times. The slow electron density is obtained from the hybrid fluid-MC simulations of ref. [22].

slowly and at 50 μs, they have become negligible in the discharge, while the elastic and (e–e) collision rates reach practically the same level. Note that the elastic collision and the (e–e) collision rates have dropped about 6 and 3 orders of magnitude respectively, since the end of the pulse at 10 μs. From Fig. 1, σ_{e-e} and σ_{ela} are higher than σ_{exc} and σ_{ion} at low energies and moreover at energies below 15 eV σ_{exc} and σ_{ion} are virtually zero, as the energy is below or near the threshold energy for ionization and excitation.

The electron energy, averaged over all electrons and over the whole plasma cell, is plotted versus time, during and after the pulse. Note that this averaging is done by weighting by the electron density of MC and slow electrons at each point of the cell in order to obtain the real average energy of all those electrons. At this point it is necessary to differentiate between MC electrons, which were already defined as the electrons created at the cathode and emitted as secondary electrons (γ emission) or by ionization collisions in the plasma, which gain high energies due to the electric field, and the so-called fluid slow electrons, which are also created at the cathode but they have lost their energy as a result of collisions in the plasma, reaching energies in this way lower than the threshold for inelastic collisions. In our work, this fluid slow electron population is very important in order to determine the thermalization energy. The term "fluid slow electron density" used in the next section represents the density of bulk plasma electrons previously calculated in a fluid model [22] and imported in our model as external data.

As can be observed in Fig. 4, the average electron energy is about 14 eV at 3 μs and it decreases until 4–5 eV at the end of the pulse (10 μs). Subsequently, the average energy exhibits a small increase which lasts less than 5 μs and afterwards it decreases significantly. After 40 μs, the average energy remains practically constant, oscillating around a value which has been estimated as 0.12 eV (see insert in Fig. 4). Therefore, the calculated thermal electron energy is considered as $<E_{thermal}>$ ~0.12 eV, and the electrons seem to thermalize within about 40–50 μs. This value is a bit less than the values reported by Biondi [41] and Surmeian [42] of about 100 μs, but it is in the same order of magnitude, and of course it depends on the operating conditions, such as discharge voltage, pulse parameters, gas pressure and therefore the kind of plasma formed. Moreover, the average energy found for the thermalized electrons is close to the values reported by Surmeian [42], i.e., in the range of 0.11–0.48 eV, and to the value obtained by Alkaa et al [35], from a Maxwellian distribution with a mean energy of 0.2 eV.

3.2. MC and slow electron energy and densities and ionization degree in the plasma

In the previous section the average electron energy considering the densities of each electron group in the cell has been calculated to obtain an absolute average energy of all electrons. In a further step the spatial distributions of the average electron energies and the density profiles of the MC and slow electrons were studied. Fig. 5 illustrates the calculated spatial distribution of the average electron energy which was also calculated taking into account all electrons (from MC and fluid model) but without weighting by the electron density of both groups. Data regarding only one half of the cylindrical plasma is shown because it is identical to the other half owing to the rotational symmetry of the plasma. Note that $r=0$ corresponds to the symmetry axis of the cylindrical cell. From these graphs it is clear how the MC electrons are constricted to the cathode dark space (CDS). Along the first 25 μs the average energy exhibits a very similar spatial distribution: the most energetic electrons are located just a few mm in front of the cathode, reaching energies up to 1200 eV (at 10 μs). In the rest of the plasma cell, the energies are very similar, and they are always lower than 100 eV. From 10 μs to 35 μs, the maximum energy is reduced by a factor of about 2 every 5 μs and the spatial distributions show a similar shape. However, at 40 μs the maximum energy drops by a factor 50 and the spatial distribution changes its shape. The negligible electric field at times longer than 35 μs reduces the typical differences between the different regions in the discharge, i.e., the subdivision into CDS and negative glow (NG) disappears. In front of the cathode a "continuum distribution" of energies exists and the energetic differences between this zone and the rest of the cell are about 0.1–0.05 eV.

In order to obtain a better understanding of the electron density evolution with time in the discharge, we plotted the MC and slow electron densities as a function of axial distance from the cathode, averaged over all radial positions. Note that the slow electron densities are not calculated in this work, but they were adopted from the hybrid fluid — MC simulations [22].

Results are shown in Fig. 6 illustrating that the MC electron density is higher than the slow electron density only at the beginning of the discharge (i.e., in the first 3 μs) and it drops afterwards as the MC electrons are gradually transferred to the slow electron group. In the afterglow, the densities of both groups decrease, although the MC electrons experience a greater reduction. At 30 μs, the MC electron density is 5 orders of magnitude lower than the corresponding density calculated during the discharge (i.e. at 5 μs). This low value indicates that the MC electrons are about to be thermalized, and that the mean electron energy is close to the bulk plasma energy. The thermalized electron energy was calculated in the last section as 0.12 eV, while the bulk plasma energy is considered to be 0.06 eV ($3/2\ k_{Boltmann}\ T_{gas}$) at T_{gas} ~725 K.

As an immediate effect of the variations of the electron densities, the ionization degree in the plasma must be affected as well. A glow discharge is a weakly ionized plasma, and normally the ionization degree is about 10^{-5} [43]. One of the most important characteristics of the dc pulsed discharge is that the degree of ionization is higher than in the continuum mode [44]. In Fig. 7 the calculated ionization degree is plotted at different times during the pulse and in the afterglow, as a function of the axial position in the plasma cell.

It is clear that the ionization degree increases from the beginning, when the voltage is applied, until the end of the pulse at 10 μs. Then the ionization degree drops to become negligible in the afterglow (as we could expect from the previous results). As far as the spatial variation is concerned, the ionization degree reaches a maximum at about 0.25 cm from the cathode and it decreases at longer distances, the drop being more pronounced in the afterglow. During the pulse (at 5 and 10 μs) and in the beginning of the afterglow (voltage is not yet zero), the ionization degree is about 10^{-4}–10^{-3}, demonstrating the above mentioned important ionization capability of a pulsed GD.

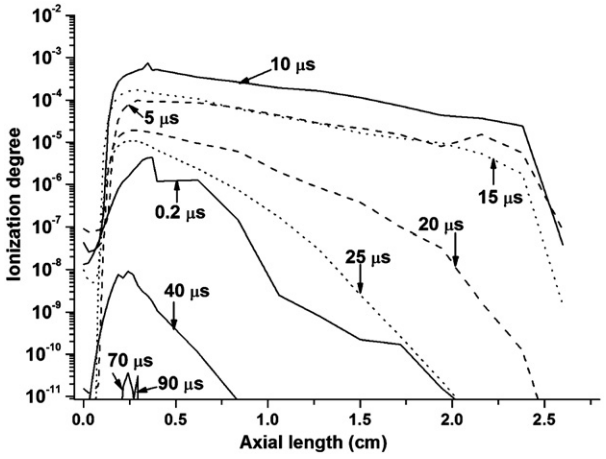

Fig. 7. Ionization degree calculated in the discharge as a function of the axial distance from the cathode position, at different times (during and after the pulse).

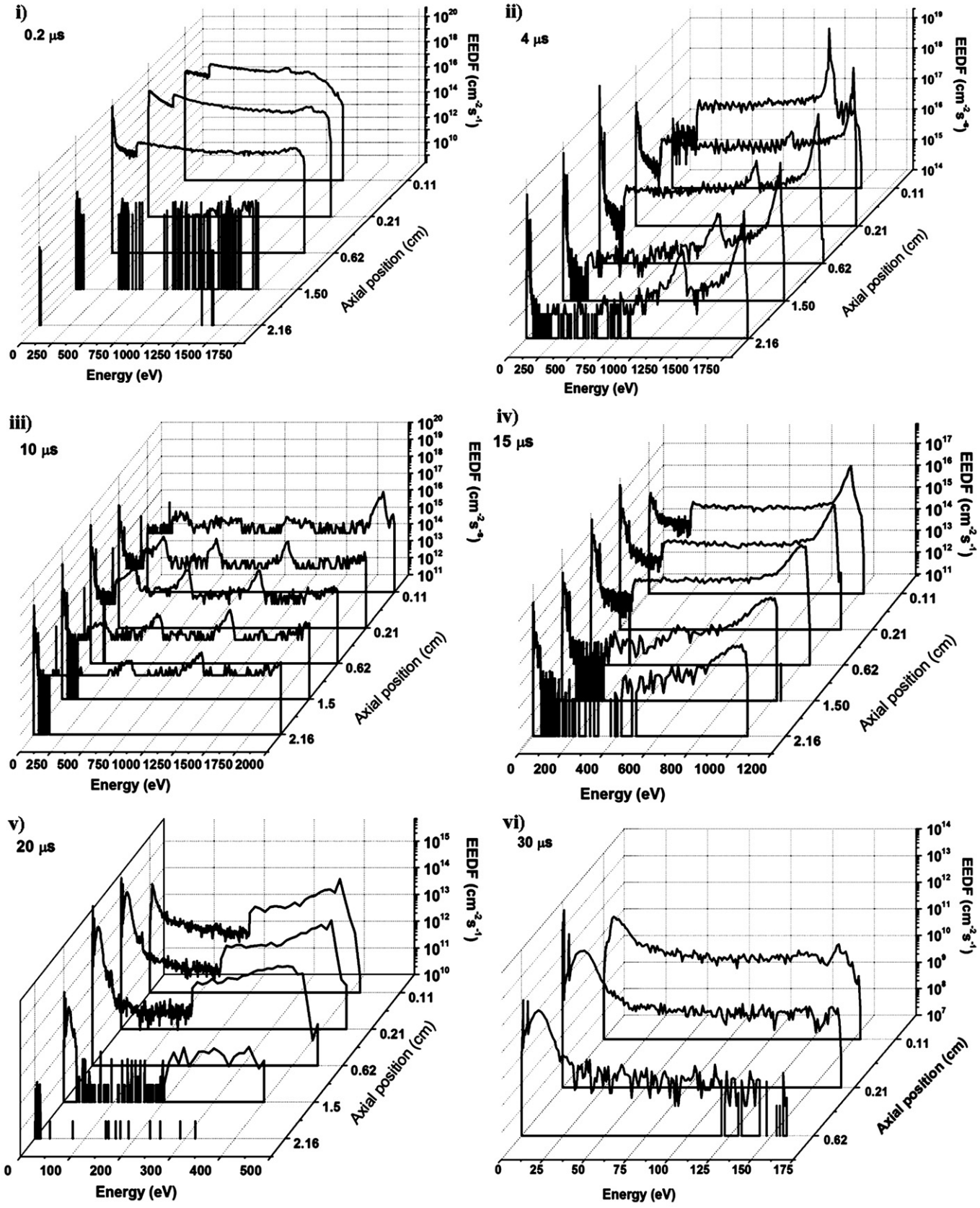

Fig. 8. Evolution of the EEDF's with the distance to the cathode at different times.

3.3. Electron energy distribution functions (EEDF's)

In this section the flux energy distribution of the MC electrons throughout the discharge at several conditions is investigated. Fig. 8 shows our results for the EEDF evolution at six fixed discharge times (i.e., 0.2, 4, 10, 15, 20, and 30 μs) as a function of five different axial positions (0.11, 0.21, 0.62, 1.50, and 2.16 cm) from the cathode. Longer times in the afterglow could not be included due to the low statistics observed for the MC electrons.

If we examine the EEDF's, in Fig. 8 i) just when the plasma is ignited (at t=0.2 μs), the MC electrons emitted by the cathode are located mainly in the CDS and in the beginning of the NG region (up to about 0.6 cm from the cathode). Moreover, in the NG, the EEDF's are characterized by a high peak corresponding to a few eV and they decay exponentially for higher energies. This initial peak, which is only observed in the NG, is attributed to electrons that lose their energy more efficiently in this region. Furthermore, the maximum energy reached in the NG by the electrons is higher than in the CDS because they can gain all possible energy from the electric field. During the pulse, at 4 μs (Fig. 8 ii), besides that peak already discussed at low energies, which is only seen in the NG, another peak located at the maximum energy is observed in the EEDF's, in the NG. This peak is attributed to the fraction of electrons that have not experienced any collision. In the CDS, there exist also such electrons, but they do not yet have the maximum possible energy, corresponding to the total discharge voltage, as they have not yet traversed the entire CDS. Hence, they have not yet gained all possible energy from the electric field, associated with this potential drop. At the end of the pulse (Fig. 8 iii) the peak observed in the NG at the maximum energy is not so intense as during the pulse (e.g. at 4 μs). The range of energy is now practically the same in both CDS and NG, but the peak at low energies is again only observed in the NG, because in this region the electrons have lost already a larger fraction of their energy by collisions. However, in the early afterglow, i.e. at 15 μs (Fig. 8 iv), the behavior of the EEDF's in the CDS and NG is quite similar. Indeed, the peak observed at low energies is now also detected in the CDS, although it is less intense. So the fraction of electrons that can undergo a collision, losing their energy, is still higher in the NG. Moreover, the energy range reached in the CDS and NG is also the same, with a peak appearing just at the maximum energy in the EEDF's. As the time goes on in the discharge, the differences between CDS and NG are reduced, and in the afterglow, e.g. at 30 μs (Fig. 8 vi), we can observe practically the same distribution at all positions. Of course, at these times the electron population has dropped dramatically far away from the cathode. The explanation for the evolution in the EEDF's in the afterglow is related to the negligible electric field in the discharge, which is basically the same in the CDS and NG.

4. Conclusions

The electron thermalization in the afterglow of a pulsed dc discharge has been studied here from collision rates, average electron energy and electron densities calculated in a MC treatment. The afterglow is characterized by a low voltage, low electrical current and so, a low electric field. Importantly the (e–e) collisions, which can be neglected in the model during the pulse, certainly need to be treated, because they are comparable to the elastic collisions in the afterglow, and both processes are in fact the only ones in the afterglow. Thus, we have developed a MC model incorporating such (e–e) collisions. In the present simulations of a 10 μs pulse width discharge, the thermalization time was found to be about 50 μs, with an average thermalization energy around 0.12 eV. We have also characterized the discharge time evolution (i.e., during the pulse, in the early and late afterglow) with respect to the average electron energy spatial distribution in the cell. The distributions show a similar behavior from the plasma ignition up to about 35 μs: the most energetic electrons are located a few millimeters in front of the cathode (corresponding to the CDS). In the rest of the cell the electrons exhibit lower energies. From 40 μs on, the distinction between the CDS and NG disappears, and the electrons are practically thermalized in the entire discharge cell, as the electric field has become negligible. We have also examined the EEDFs at several times and axial positions from the cathode. The common characteristics found in the dc continuum discharge are also observed in the pulsed mode during the pulse ($t \leq 10$ μs): in the CDS, electrons gain energy from the electric field as they travel towards the NG, thereby losing also some energy as a result of collisions. In the NG the electrons have gained all energy equal to the total voltage drop over the CDS, but on the other hand, they lose their energy also more efficiently by collisions. Consequently, a peak at a few eV is detected in the EEDF's in the NG. Nevertheless, an intense peak located at the maximum electron energy is also observed in the NG, indicating that an important fraction of electrons have not undergone any collision. In the CDS this peak is placed at somewhat lower energy, as the electrons have not yet gained all energy equal to the total voltage drop.

In the afterglow the differences between CDS and NG disappear gradually, and at 30 μs there is no distinction between CDS and NG, i.e., the EEDF's are practically the same, as it was also demonstrated for the spatial electron energy distributions.

Acknowledgements

Financial support from "Plan Nacional de I+D+I" (Spanish Ministry of Education and Science, and FEDER Programme) through the project MAT2007-65097-C02 is gratefully acknowledged. A. Martin is indebted to the Spanish Ministry of Education and Science for a grant (FPI) associated to the MAT2003-09243-C02 project. A. Bogaerts would like to acknowledge financial support from the European Marie Curie Research Training Network GLADNET (Analytical Glow Discharge Network).

References

[1] W. Hang, C. Baker, B.W. Smith, J.D. Winefordner, W.W. Harrison, Microsecond-pulsed glow discharge time-of-flight mass spectrometry: analytical advantages, J. Anal. At. Spectrom. 12 (1997) 143–149.
[2] F.L. King, W.W. Harrison, Glow discharge mass spectrometry: an introduction to the technique and its utility, Mass Spectrom. Rev. 9 (1990) 285–317.
[3] C. Yang, K. Ingeneri, W.W. Harrison, A pulsed Grimm glow discharge as an atomic emission source, J. Anal. At. Spectrom. 14 (1999) 693–698.
[4] A. Bengtson, C. Yang, W.W. Harrison, Microsecond pulsed glow discharge optical emission spectrometry-investigation of temporal emission characteristics, J. Anal. At. Spectrom. 15 (2000) 1279–1284.
[5] S. Potapov, E. Izrailov, V. Verzigova, M. Voronov, S. Suprunovich, M. Slyadnev, A. Ganeev, Pulsed glow discharge in thin-walled metallic hollow cathode. Analytical possibilities in atomic and mass spectrometry, J. Anal. At. Spectrom. 18 (2003) 564–571.
[6] W.O. Walden, W.W. Harrison, B.W. Smith, J.D. Winefordner, Multi-element glow discharge atomic fluorescence using continuum source, J. Anal. At. Spectrom. 9 (1994) 1039–1043.
[7] A. Martin, R. Pereiro, N. Bordel, A. Sanz-Medel, Microsecond pulsed versus direct current glow discharge as ion sources for analytical glow discharge-time of flight mass spectrometry, J. Anal. At. Spectrom. 22 (2007) 1179–1183.
[8] C. Yang, W.W. Harrison, Investigation of a novel hollow cathode configuration for Grimm-type glow discharge emission, Spectrochim. Acta Part B 56 (2001) 1195–1208.
[9] C.L. Lewis, L. Lei, J. Thomas Mil, la y, S. Downey, J. Warrick, F.L. King, Temporal emission characteristics of millisecond pulsed radio frequency and direct current glow discharges, J. Anal. At. Spectrom. 18 (2003) 527–532.
[10] C.L. Lewis, E.S. Oxley, C.K. Pan, R.E. Steiner, F.L. King, Determination of $^{40}Ca^{+}$ in the presence of $^{40}Ar^{+}$: an illustration of the utility of time-gated detection in pulsed glow discharge mass spectrometry, Anal. Chem. 71 (1999) 230–234.
[11] W. Hang, W.O. Walden, W.W. Harrison, Microsecond pulsed glow discharge as an analytical spectroscopic source, Anal. Chem. 68 (1996) 1148–1152.
[12] C.L. Lewis, M.A. Moser, W. Hang, D.E. Dale Jr, D.C. Hassell, V. Majidi, Influence of discharge parameters on real-time chemical speciation for gas chromatography pulsed glow discharge plasma time-of-flight mass spectrometry, J. Anal. At. Spectrom. 18 (2003) 629–636.
[13] V. Majidi, M. Moser, C. Lewis, W. Hang, F.L. King, Explicit chemical speciation by microsecond pulsed glow discharge time-of-flight mass spectrometry: concurrent acquisition of structural, molecular and elemental information, J. Anal. At. Spectrom. 15 (2000) 19–25.
[14] E. Oxley, C. Yang, W.W. Harrison, Quantitative depth analysis using microsecond pulsed glow discharge atomic emission spectrometry, J. Anal. At. Spectrom. 15 (2000) 1241–1245.

[15] M. Hohl, A. Kanzari, J. Michler, T. Nelis, K. Fuhrer, M. Gonin, Pulsed r.f-glow-discharge time-of-flight mass spectrometry for fast surface and interface analysis of conductive and non-conductive materials, Surf. Interface Anal. 38 (2006) 292–295.
[16] A. Martin, R. Pereiro, N. Bordel, A. Sanz-Medel, Improvement of depth resolution for the analysis of thin layered materials using microsecond pulsed glow discharge time-of-flight mass spectrometry, ECASIA'07, 12th European Conference on Applications of Surface and Interface Analysis, Brussels, September 9-14 2007.
[17] X.B. Tian, P.K. Chu, Experimental investigation of the electrical characteristics and initiation dynamics of pulsed high-voltage glow discharge, J. Phys., D. Appl. Phys. 34 (2001) 354–359.
[18] J.A. Strauss, N.P. Ferreira, H.G.C. Human, An investigation into the role of metastable argon atoms in the afterglow plasma of a low pressure discharge, Spectrochim. Acta Part B 37 (1982) 947–954.
[19] G.P. Jackson, F.L. King, Bulk plasma properties in the pulsed glow discharge, Spectrochim. Acta Part B 58 (2003) 1417–1433.
[20] F.L. King, C. Pan, Temporal signal profiles of analytical species in modulated glow discharge plasmas, Anal. Chem. 65 (1993) 735–739.
[21] A. Bogaerts, The afterglow mystery of pulsed glow discharges and the role of dissociative electron-ion recombination, J. Anal. At. Spectrom. 22 (2007) 502–512.
[22] A. Bogaerts, R. Gijbels, Hybrid Monte Carlo-fluid model for a microsecond pulsed glow discharge, J. Anal. At. Spectrom. 15 (2000) 895–905.
[23] A. Bogaerts, R. Gijbels, Modelling of a microsecond pulsed glow discharge: behaviour of the argon excited levels and of the sputtered copper atoms and ions, J. Anal. At. Spectrom. 16 (2001) 239–249.
[24] A. Bogaerts, R. Gijbels, G.P. Jackson, Modeling of a millisecond pulsed glow discharge: investigation of the afterpeak, J. Anal. At. Spectrom. 18 (2003) 533–548.
[25] R.J. Carman, A simulation of electron motion in the cathode sheath region of a glow discharge in argon, J. Phys., D. Appl. Phys. 22 (1989) 55–66.
[26] E. Eggarter, Comprehensive optical and collision data for radiation action. II. Ar^+, J. Chem. Phys. 62 (1975) 833–847.
[27] W.C. Fon, K.A. Berrington, P.G. Burke, A. Hibbert, The elastic scattering of electrons from inert gases. III. Argon, J. Phys. B: At. Mol. Opt. Phys. 16 (1983) 307–321.
[28] A.V. Phelps, Z.L. Petrovic, Cold-cathode discharges and breakdown in argon: surface and gas phase production of secondary electrons, Plasma Sources Sci. Technol. 8 (1999) R21–R44.
[29] F.J. Mehr, M.A. Biondi, Electron-temperature dependence of electron-ion recombination in Argon, Phys. Rev. 176 (1968) 322–326.
[30] Y.J. Shiu, M.A. Biondi, Dissociative recombination in argon: dependence of the total rate coefficient and excited-state production on electron temperature, Phys. Rev. A. 17 (1978) 868–872.
[31] M.A. Biondi, Applied atomic collision physics, volume 3: gas lasers, in: E.W. McDaniel, W.L. Nighan (Eds.), Electron-Ion Recombination in Gas Lasers, Academic press, New York, 1982, pp. 173–189.
[32] M. Surendra, D.B. Graves, G.M. Jellum, Self-consistent model of a direct-current glow discharge: treatment of fast electrons, Phys. Rev. A 41 (1990) 1112–1125.
[33] Y. Weng, M.J. Kushner, Method for including electron–electron collisions in Monte Carlo simulations of electron swarms in partially ionized gases, Phys. Rev. A 42 (1990) 6192–6200.
[34] M. Yousfi, A. Himoudi, A. Gaouar, Boltzmann equation and Monte Carlo analysis of electron–electron interactions on electron distributions in nonthermal cold plasmas, Phys. Rev. A 46 (1992) 7889–7901.
[35] A. Alkaa, P. Ségur, A. Zahraoui, M. Kadri-H, Monte Carlo treatment of the transport of electrons in a gas including electron–electron interactions, Phys. Rev. E 50 (1994) 3006–3020.
[36] A. Alkaa, doctorat de l'Université Paul Sabatier, No. 967, Univeristé Paul Sabatier, 1991.
[37] J.A. Bittencourt, Fundamentals of Plasma Physics, Pergamon Press, New York, 1986.
[38] Y.A. Schreider, The Monte Carlo Method, Pergamon Press, NewYork, 1966.
[39] Ales Fiala, doctorat de l'Université Paul Sabatier, No. 2059, Université Paul Sabatier, 1995.
[40] A. Bogaerts, R. Gijbels, V.V. Serikov, Calculation of gas heating in direct current argon glow discharges, J. Appl. Phys. 87 (2000) 8334–8344.
[41] M.A. Biondi, Diffusion, de-excitation, and ionization cross sections for metastable atoms I, Phys. Rev. 88 (1952) 660–665.
[42] A. Surmeian, C. Dip, la su, C.B. Collins, G. Musa, I-Iovitz Popescu, Electron temperature measurements in the afterglow plasma of a high-voltage pulsed discharge in caesium vapours, J. Phys. D: Appl Phys. 30 (1997) 1755–1758.
[43] A. Bogaerts, E. Neyts, R. Gijbels, J. van der Mullen, Gas discharge plasmas and their applications, Spectrochim. Acta Part B 57 (2002) 609–658.
[44] W.W. Harrison, Pulsed glow discharge as a solids analysis source, J. Anal. At. Spectrom. 13 (1998) 1051–1056.